Journal of Solid State Chemistry 187 (2012) 309–315

Contents lists available at SciVerse ScienceDirect

Journal of Solid State Chemistry

journal homepage: www.elsevier.com/locate/jssc

Response of intergrown microstructure to an electric field and its consequences in the lead-free piezoelectric bismuth sodium titanate

Yun Liu [a,*], Lasse Norén [a], Andrew J. Studer [b], Ray L. Withers [a], Yiping Guo [a], Yongxiang Li [c], Hui Yang [a,d], Jian Wang [a]

[a] Research School of Chemistry, the Australian National University, ACT 0200, Australia
[b] Bragg Institute, the Australian Nuclear Science & Technology Organisation, Locked Bag 2001, Kirrawee DC NSW 2232, Australia
[c] State Key Laboratory of High Performance Ceramics and Superfine Microstructures, Shanghai Institute of Ceramics, Chinese Academy of Sciences, Shanghai 200050, China
[d] College of Life Science & Technology, Shaanxi University of Science & Technology, Xian 710021, China

ARTICLE INFO

Article history:
Received 12 September 2011
Received in revised form
9 January 2012
Accepted 15 January 2012
Available online 25 January 2012

Keywords:
Bismuth sodium titanate
Intergrown microstructure
Neutron diffraction
Electron diffraction

ABSTRACT

We investigate the *R*3*c* average structure and micro-structure of the ceramic $Bi_{0.5}Na_{0.5}TiO_3$ (BNT) *in situ* under applied electric fields using diffraction techniques. Electron diffraction implies the presence of significant octahedral tilt twin disorder, corresponding to the existence of a fine scale intergrown microstructural (IGMS) 'phase' within the *R*3*c* rhombohedral average structure matrix. A careful neutron refinement suggests not only that the off-centre displacements of the cations relative to the oxygens in the *R*3*c* regions increases systematically on application of an electric field but also that the phase fraction of the IGMS regions increases systematically. The latter change in phase fraction on application of the electric field enhances the polar displacement of the cations relative to the oxygen anions and affects the overall strain response. These IGMS regions form local polar nano regions that are not correlated with one another, resulting in polarisation relaxation and strain behaviour observed in BNT-containing materials.

1. Introduction

The $Pb(Zr_{1-x}Ti_x)O_3$ (PZT) system exhibits strong electro-mechanical coupling and a large piezo-response when its chemical composition is situated closest to the morphotropic phase boundary (MPB) region separating rhombohedral ferroelectric from tetragonal ferroelectric regions in the phase diagram. Electro-mechanical coupling is enhanced even further when the chemical composition of the system being investigated is situated close to a triple point separating a cubic paraelectric phase from rhombohedral ferroelectric and tetragonal ferroelectric phases as occurs in the case of the $(1-x)Ba(Ti_{0.8}Zr_{0.2})O_{3-x}(Ba_{0.7}Ca_{0.3})TiO_3$ system [1], resulting in an extremely high piezoelectric response. It is thus well recognised [2] that electro-mechanical coupling is optimal in the vicinity of MPB's, phase transition regions across which the direction of ferroelectric displacement changes abruptly.

Bismuth sodium titanate of nominal composition $Bi_{0.5}Na_{0.5}TiO_3$ (BNT), however, is reported not to be near any such structural phase transition, to be single phase and to have a ferroelectric, rhombohedral *R*3*c* structure at ambient temperature [3] (see e.g., Fig. 1(a)). Nonetheless, it is also a material that exhibits promising piezoelectric properties [4] e.g., a high piezoelectric coefficient (~91 pC/N), a high electro-mechanical coupling coefficient k_{33} (~0.47) and a high Curie temperature, T_C (~320 °C). These properties are comparable with those of existing lead-free piezoelectric solid solutions with chemical compositions close to MPB's. While the relationship between synthesis conditions, dopant concentration and the physical properties of BNT have been extensively investigated [5–7], there has yet to be an *in situ* investigation of the structural, especially the intergrown structural, evolution of the ambient temperature form under an applied external electric field. In this study, we therefore report the results of a careful neutron powder diffraction study of a ceramic BNT sample *in situ* under a range of applied electric fields. The evolution of the intergrown microstructure (IGMS) and its consequences as regards the direction and ease of ion displacements in this compound are investigated. Electron diffraction patterns are also collected to provide complimentary evidence to support the arguments given.

2. Experimental

The BNT ceramics used were synthesised via solid state reaction. The detailed processing conditions used are reported

* Corresponding author.
E-mail address: yliu@rsc.anu.edu.au (Y. Liu).

0022-4596/$ - see front matter © 2012 Elsevier Inc. All rights reserved.
doi:10.1016/j.jssc.2012.01.027

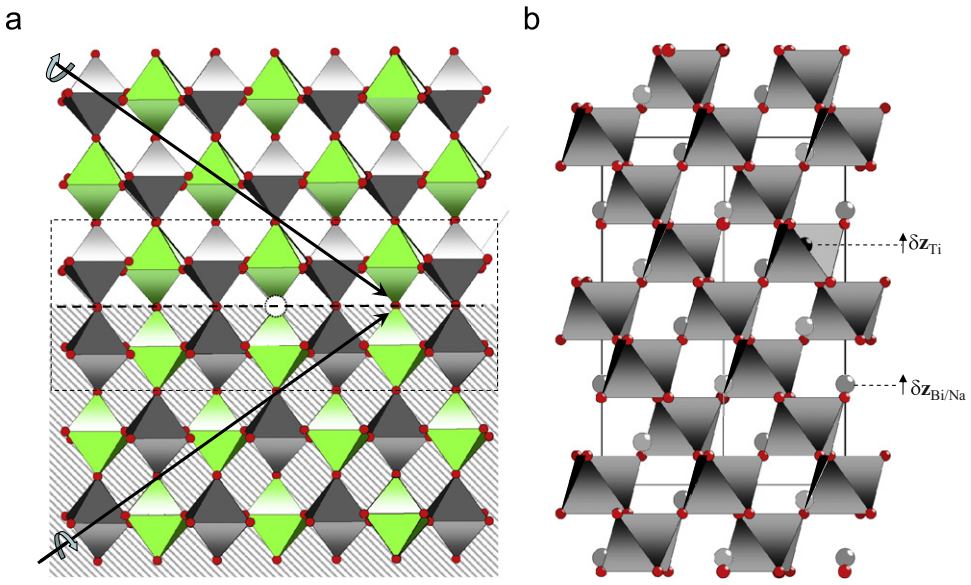

Fig. 1. (a) Schematic drawing of two orientation domains (grey hatched and non-hatched) of the rhombohedral *R3c* structure of BNT related with a twin plane (the thick dashed line inside of the dash-line frame). The average rhombohedral structure of BNT is composed of titanium –centred octahedral framework (ReO_3 structure type) with different rotations patters and filled A-site cations (just one atom given as reference). The arrows show two different octahedral tilt-rotations of the parent perovskite sub-structure around the $[1\,1\,1]_p$ direction. Note that the twin boundary, inside the dashed box has a different structure and space group than either of the two domains. Part(b) shows how the cations move off their central position relative to the oxygen anions along the resultant $\mathbf{c}_h$ direction. (a) ReO_3 and (b) 3KV structure.

in Ref. [8]. The resultant pellets were polished down to 0.6 mm thickness and their surfaces coated by silver paste to form a parallel-plate-capacitor-type sandwich structure for electrical property characterisation and neutron diffraction study *in situ* under an applied electric field.

The neutron diffraction data collection was performed at the OPAL reactor at the Australian Nuclear Science and Technology Organisation (ANSTO) using Wombat, the high intensity powder diffraction instrument. A germanium monochromator with (1,1,5) at the face and (1,−1,0) perpendicular was oriented to use the (1,1,3) reflection at a takeoff angle of 90°, producing a wavelength of 2.41 Å. The sample was placed on a boron nitride sample holder with a vanadium wire spring supplying the voltage pushing the sample against a vanadium earth plate. The electric field was applied along the direction perpendicular to the sample surface with values of 0, 8.3, 16.6, 33.3 and 50 kV/cm, respectively (corresponding to applied voltages of 0, 0.5, 1, 2 and 3 kV). The original data was treated in such a way as to get rid of the distortion of the peak profile affected by the Wombat area detector geometry. The direction normal to the surface of the sample is oriented parallel to the incident neutron beam to obtain the highest intensity for better structural analysis. After the above neutron data were completed, electron diffraction patterns (EDP's) of BNT were collected at room temperature using a Philips EM 430 Transmission Electron Microscope (TEM) operating at 300 kV on crushed grains of the sample (from the same pellet) dispersed onto holey carbon-coated copper grids.

3. Preliminary structural considerations

The rhombohedral *R3c* structure reported for $Bi_{0.5}Na_{0.5}TiO_3$ (BNT) at room temperature[3] ($\mathbf{a}_h=-\mathbf{b}_p+\mathbf{c}_p$, $\mathbf{b}_h=-\mathbf{c}_p+\mathbf{a}_p$, $\mathbf{c}_h=2(\mathbf{a}_p+\mathbf{b}_p+\mathbf{c}_p)$, $\mathbf{a}_h^*={}^1/_6[2,-4,2]_p^*$, $\mathbf{b}_h^*={}^1/_6[4,-2,-2]_p^*$, $\mathbf{c}_h^*={}^1/_6[1\,1\,1]_p^*$; subscript h for the rhombohedral cell in the hexagonal setting, subscript p for the parent perovskite cell) can be described in terms of an $a^-a^-a^-$ octahedral tilt rotation of the parent perovskite sub-structure around the $[1\,1\,1]_p$, or $\mathbf{c}_h$, direction (giving rise to $\mathbf{G}\pm{}^1/_2[1\,1\,1]_p^*$ satellite reflections, **G** a parent perovskite sub-structure reflection). The resultant octahedral tilt rotation pattern is shown in the upper and lower thirds of Fig. 1(a) (the regions outside the dashed rectangular frame). This octahedral tilt rotation is accompanied by off-centred shifts of the Bi/Na and Ti ions relative to the oxygen ions along the resultant $\mathbf{c}_h$ direction (shown in Fig. 1(b)). These latter, $z_{Bi/Na}\mathbf{c}_h$ and $z_{Ti}\mathbf{c}_h$, off-centre shifts relative to the oxygen anion array are responsible for the ferroelectric behaviour of BNT at room temperature (a recent re-refinement of BNT at room temperature [9] suggests that the Bi ions also have a disordered displacive component perpendicular to $[1\,1\,1]_p$ or $\mathbf{c}_h$). For the purposes of this refinement, however, we have ignored this disordered displacive component as we do not wish to over-parameterize the structural model and are primarily interested in trends in field-induced atomic structural changes in the above structural parameters. For the same reason z_{Bi} and z_{Na} were also constrained to be equal. There are then only four independent fractional co-ordinate parameters to be refined (as defined in Table 1 of Jones and Thomas in Ref. 3).

4. *In situ* neutron diffraction

Structure models were refined against neutron diffraction data using the programme package Rietica [10]. The non-structural parameters refined were the background (using a Chebyshev II polynomial with 6 refineable parameters), scale factors, a zero point shift and peak shape parameters. The structural parameters refined were the unit cell parameters $\mathbf{a}_h$ and $\mathbf{c}_h$ and the four independent fractional co-ordinate parameters described above, following Table 1 of Jones and Thomas [3]. Isotropic atomic displacement parameters were initially taken from literature values, although these parameters were refined at a later stage to check the behaviour of the refinement.

A small amount (~2–3% sample volume) of a contaminant phase with nominal composition ~"$Na_{0.33}Bi_{3.54}Ti_3O_{11.48}$" was found via electron probe micro-analysis (EPMA) analysis of the sample which could not be observed in the conventional X-ray diffraction pattern. The very weak additional peaks in the diffraction patterns that are likely to originate from this phase were

Table 1
A comparison between the refinements using different models: rhombohedral phase without PO (Model 1) and with (Model 2), as well as rhombohedral+cubic phases without PO (Model 3) and with (Model 4). The symbol (*) means that the sample have been cycled from 3 kV back to 0 kV. R_p and R_{wp} are the profile and the weighted profile to be used to estimate the agreement between the observations and the model during the course of the refinement.

Parameters	0 kV	0.5 kV	1 kV	2 kV	3 kV	0 kV*	Comment
z (Bi^{3+}/Na^{+})	0.2641(9)	0.2637(9)	0.2643(10)	0.2730(5)	0.2832(7)	0.2747(6)	Model 1
	0.2641(9)	0.2637(9)	0.2645(9)	0.2725(5)	0.2816(5)	0.2740(4)	Model 2
	0.2640(10)	0.2636(9)	0.2644(10)	0.2786(9)	0.2932(12)	0.2806(9)	Model 3
	0.2641(9)	0.2638(9)	0.2648(9)	0.2753(5)	0.2840(6)	0.2815(11)	Model 4
z (Ti^{4+})	0.0041(15)	0.0024(16)	0.0038(15)	0.0081(8)	0.0147(12)	0.0091(11)	Model 1
	0.0047(15)	0.0027(16)	0.0045(15)	0.0088(8)	0.0194(9)	0.0113(7)	Model 2
	0.0034(17)	0.0020(16)	0.0034(16)	0.0081(9)	0.0196(12)	0.0115(11)	Model 3
	0.0041(16)	0.0024(16)	0.0040(16)	0.0092(9)	0.0196(8)	0.0144(9)	Model 4
x(O^{2-})	0.1205(14)	0.1199(14)	0.1202(14)	0.1227(9)	0.1308(13)	0.1229(10)	Model 1
	0.1213(14)	0.1216(13)	0.1212(13)	0.1223(8)	0.1211(11)	0.1223(8)	Model 2
	0.1189(15)	0.1187(14)	0.1185(15)	0.1222(8)	0.1224(14)	0.1164(13)	Model 3
	0.1200(15)	0.1199(14)	0.1192(15)	0.1162(10)	0.1106(12)	0.1028(38)	Model 4
y(O^{2-})	0.3265(26)	0.3261(26)	0.3256(26)	0.3294(14)	0.3304(19)	0.3297(17)	Model 1
	0.3275(26)	0.3278(25)	0.3268(25)	0.3294(13)	0.3259(15)	0.3303(14)	Model 2
	0.3255(28)	0.3258(26)	0.3252(27)	0.3293(14)	0.3334(18)	0.3317(16)	Model 3
	0.3267(27)	0.3267(26)	0.3260(27)	0.3276(15)	0.3250(14)	0.3267(21)	Model 4
a	5.4783(5)	5.4784(5)	5.4786(5)	5.4805(4)	5.5017(11)	5.4832(6)	Model 1
	5.4780(5)	5.4783(5)	5.4783(5)	5.4895(4)	5.4922(7)	5.4792(5)	Model 2
	5.4807(8)	5.4803(8)	5.4809(8)	5.4815(12)	5.4926(15)	5.4753(10)	Model 3
	5.4800(8)	5.4797(7)	5.4808(8)	5.4785(10)	5.4951(9)	5.4747(14)	Model 4
c	13.4901(22)	13.4884(23)	13.4892(23)	13.5292(18)	13.5292(55)	13.5364(25)	Model 1
	13.4929(22)	13.4927(23)	13.4923(22)	13.5254(17)	13.5396(17)	13.5332(14)	Model 2
	13.4893(29)	13.4879(25)	13.4893(29)	13.5290(19)	13.5492(49)	13.5488(41)	Model 3
	13.4917(27)	13.4906(25)	13.4930(34)	13.5383(25)	13.5421(16)	13.5493(29)	Model 4
R_p	2.99	2.96	3.02	3.00	4.81	3.75	Model 1
	2.98	2.89	2.95	2.91	3.86	3.2	Model 2
	2.95	2.88	2.95	2.90	4.02	3.38	Model 3
	2.88	2.80	2.91	2.86	3.21	2.87	Model 4
R_{wp}	3.88	3.80	3.87	3.93	6.85	5.06	Model 1
	3.79	3.74	3.81	3.79	5.07	4.05	Model 2
	3.77	3.69	3.74	3.77	5.54	4.43	Model 3
	3.76	3.64	3.73	3.70	4.14	3.69	Model 4
GoF	5.28	5.05	5.20	5.36	16.07	8.75	Model 1
	5.14	4.88	5.04	5.01	8.87	5.61	Model 2
	4.97	4.77	4.90	4.98	10.60	6.78	Model 3
	4.89	4.67	4.87	4.80	5.95	4.74	Model 4

omitted in the Rietveld refinement as the structure is unknown and the peaks are so weak that it is impossible to solve the structure from them, although similarities with $Bi_4Ti_3O_{12}$ [11] are likely. In some cases, they could be treated as excluded regions when that was possible (c.f. Fig. 2 at $\sim$45°, $\sim$70° and $\sim$95° in 2θ highlighted by grey strips).

A second additional phase present in the pattern, but not in the sample, is that of silver originating from the silver electrodes that are necessarily coated onto the sample. Only three Ag peaks are present in the pattern. One of these peaks, however, overlaps with a sample line (see Fig. 2 at $\sim$63° in 2θ), making it important to refine the relative amount of silver in the sample i.e., the scale factor for the Ag phase. In practice, the refined scale factor for the silver phase using the various models described below did not vary by more than 0.2%. The zero point for the Ag phase is also necessarily different from that of the sample as a result of its location on the surface of the BNT sample. However, only one zero point is possible to refine at a time in the programme package used. In order to overcome this problem, we instead refined the unit cell parameter of the Ag phase, which in consequence deviated slightly from the literature value.

A visual inspection of the various patterns obtained shows that the $\mathbf{G} \pm {}^1/_2[1\ 1\ 1]^*_p$ satellite reflections are noticeably broadened relative to the parent perovskite sub-structure reflections, **G**. This implies that the superstructure (associated with $a^-a^-a^-$ octahedral tilt rotation, see Fig. 1) and the parent perovskite sub-structure have different correlation lengths. The satellite reflections were then individually fitted using Gaussian functions and the full width at half maximum (FWHM) normalised against those of the parent perovskite sub-structure reflections. This yielded values of between $\sim$1.1 and $\sim$2.4 depending on the reflections chosen. This is strongly suggestive of some form of stacking fault disorder affecting the $\mathbf{G} \pm {}^1/_2[1\ 1\ 1]^*_p$ satellite reflections but not the parent perovskite sub-structure reflections, **G**, as shown in Fig. 1(a), the hatched area, separated from the rest by a solid dash-line, represents one octahedral tilt rotation of the parent perovskite sub-structure around the $[1\ 1\ 1]_p$ direction. Two different domain orientations, with two different rotations directions, are illustrated by two arrows that terminate in the twin boundary. The characteristic streaking of the $\mathbf{G} \pm {}^1/_2[1\ 1\ 1]^*_p$ satellite reflections along the $\langle 1\ 0\ 0 \rangle^*_p$ reciprocal lattice directions all the way to the $\mathbf{G} \pm {}^1/_2[0\ 1\ 1]^*_p$ regions of reciprocal space apparent in electron diffraction patterns (see e.g., Fig. 3) is consistent with this interpretation. The arrows in Fig. 3 indicate these weak $\mathbf{G} \pm {}^1/_2[0\ 1\ 1]^*_p$ 'reflections'. It is also consistent with the results of Dorcet et al. [13–16], who have directly observed the high resolution TEM images [14] and corresponding electron diffraction patterns [15,16]. Their results have shown that such characteristic diffuse streaking arises from fine scale, pseudo-merohedral twinning of the $R3c$ structure on $[1\ 0\ 0]_p$ twin planes giving rise to an orthorhombic $a^-a^+a^-$, *Pnma* structure at the interface that is at least two octahedral layers thick (see the structure inside of the dash-line frame in Fig. 1(a)).

In order to be able to describe these effects, it would be necessary to be able to refine the parent and the satellite classes of reflections with different half-width parameters. This is, however, not possible with the Rietica programme so an alternative method was used i.e., an additional cubic parent perovskite

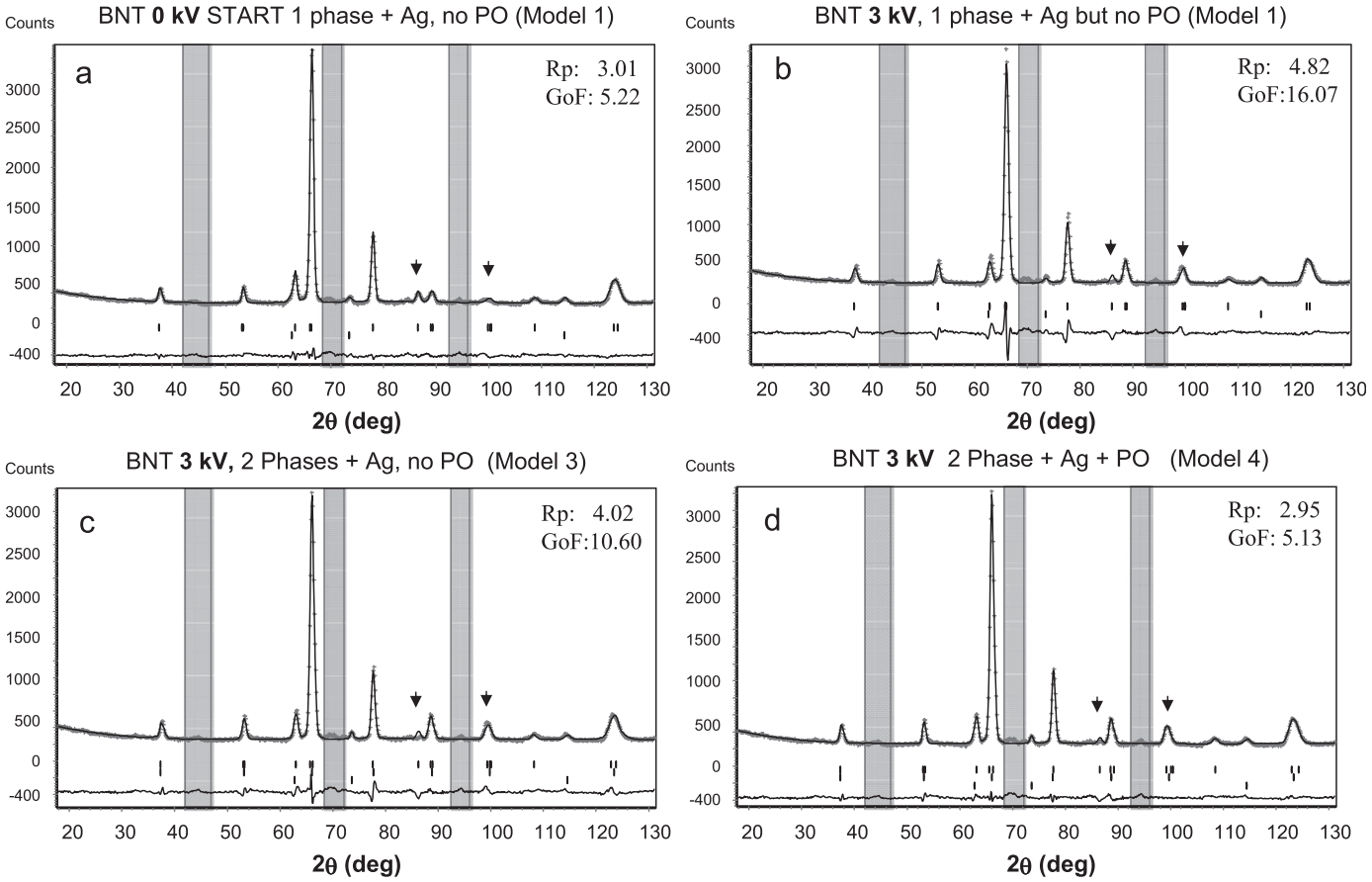

Fig. 2. The neutron diffraction patterns refined according to different considerations: an 0 kV pattern refined by Model 1 (a), as well as an 3 kV pattern refined by Model 1 (b), Model 3 (c) and Model 4 (d).

phase was introduced. The justification for this is associated with the orthorhombic $a^-a^+a^-$, *Pnma* structure (and its rotational invariants) at the various possible twin interfaces (see the hatched area in Fig. 1). Note that there is no correlation between one of these twin domain boundary regions and the next such boundary region as the thickness of the *R*3*c* superstructure domain regions vary (if they did not vary we would see diffraction evidence of additional long-range order). The average structure of these fine scale twin domain boundary regions corresponds to the superposition of all rotation invariants, the time/space average of which is a normal cubic perovskite parent structure. The presence of such an additional "cubic phase" allows us to use half-width parameters when refining the *R*3*c* superstructure phase that are in line with what is needed to describe the satellite reflections, i.e., broader, while the additional "cubic phase" then enables the parent reflections to be appropriately modelled.

Please note, that this additional "cubic" phase is just a "trick" to get around the effect of fine scale nano structural domains (i.e., IGMS) in the sample, it does not exist *per se*. Introducing this additional "cubic" phase (Model 3 and Model 4) leads to a significant improvement (Table 1 and Fig. 2(c)) when compared to Model 1 (Table 1 and Fig. 2(b)).

It is also noteworthy that the applied electric field can induce texture in the sample [17,18]. This would result in a diffraction effect similar to those modelled with preferred orientation (PO) or via "Lattice Strain Distribution Functions" (LSDFs) [19]. However, "*the construction of an LSDF from experimentally measured lattice strain data is an inherently indeterminate problem*" [19]. In this work, we are not trying to describe or analyse the texture induced by the applied electric field, instead we are comparing the relative effect on the refined structure if such an effect is allowed for, or not. This gives us four different models (see Table 1) to try out. Model 1 has only one sample phase (as well as the additional silver from the electrodes) and no preferred orientation parameters refined. The second model, Model 2, also allows for PO to be refined according to the March–Dollase Model [9]. Model 3 allows an additional cubic phase in order to allow for the effect of nano-domains, or intergrown domain boundary regions, as detailed above, but without PO while the final model, Model 4, also allows for PO to be refined.

The average structure of the overwhelmingly dominant $Na_{0.41}Bi_{0.53}TiO_3$ phase was initially refined using the *R*3*c* average structure of $Na_{0.5}Bi_{0.5}TiO_3$ reported by Jones and Thomas et al. [3,12] as a starting point. All six diffraction patterns (0 kV start, 0.5 kV, 1 kV, 2 kV, 3 kV, return to 0 kV) were refined accordingly via these four models. The difference in chemical stoichiometry suggested by EPMA analysis did not cause any problem and the standard refinements converged quickly. Table 1 summarises all the refinement parameters, including R_p, R_{wp} and GoF (goodness of fit). R_p and R_{wp} are the profile and weighted profile fits. The GoF is based on the whole diffraction pattern and is here defined as the sum of the weighted difference between an observed intensity at a point in the diffraction pattern and the calculated intensity of the same point squared; divided by the difference between the number of observations and the number of parameters refined in the Rietveld analysis [11].

From Table 1 and Fig. 2, the refinement based on Model 1 is reasonable for the diffraction patterns collected at lower voltages but become unsatisfactory for the pattern obtained at 3 kV (see Fig. 2(b) and Table 1) and also for the patterns obtained after the

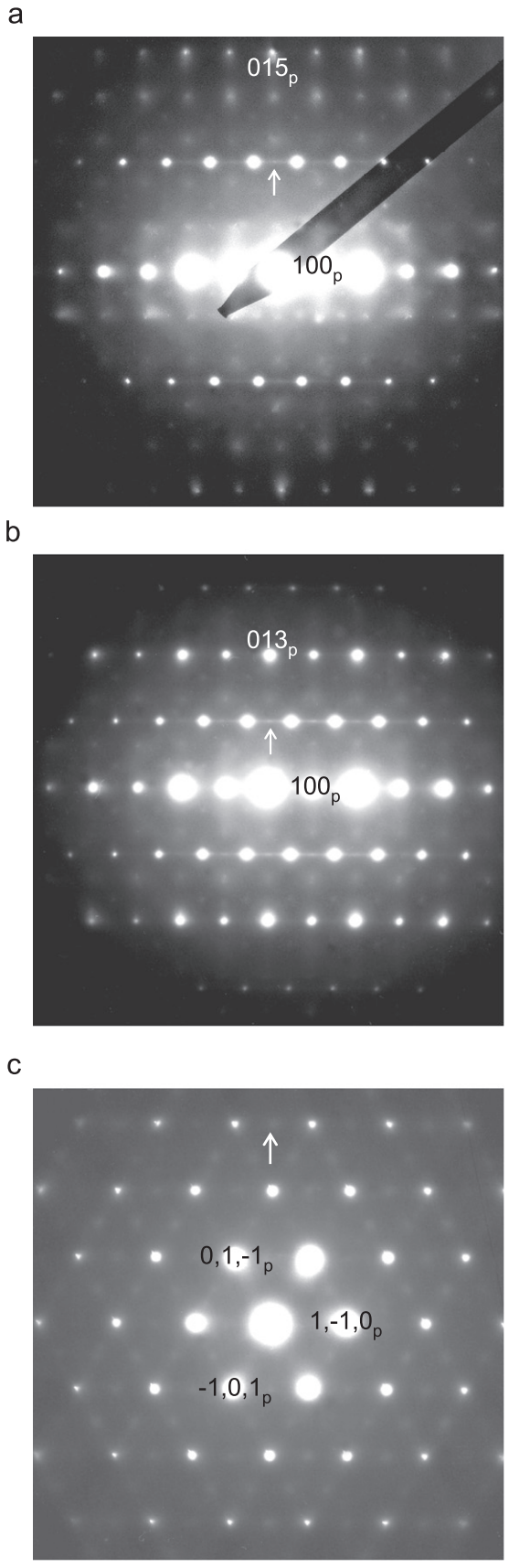

Fig. 3. Electron diffraction patterns (EDPs) of BNT collected along the zone axis $\langle 0, 5, -1 \rangle_p$ (a), $\langle 0, 3, -1 \rangle_p$ (b), and $\langle 1\,1\,1 \rangle_p$ (c) directions. The arrows indicate the weak reflections that can not be indexed with the rhombohedral phase of BNT, that actually corresponds to the ½[0 1 1] satellite reflections, originating from twinning defects giving rise to the orthorhombic *Pnma* structure.

voltage was removed, as indicated by very large GoF's. Note that the domain wall motions of a ferroelectric material under an applied electric field can be considerable and this would definitely make a contribution similar to that of preferred orientation (PO). The higher the voltage applied, the more domain wall motion occurs, leading to more obvious PO. The 3 kV voltage corresponds to an applied electric field of ~50 kV/cm that is just

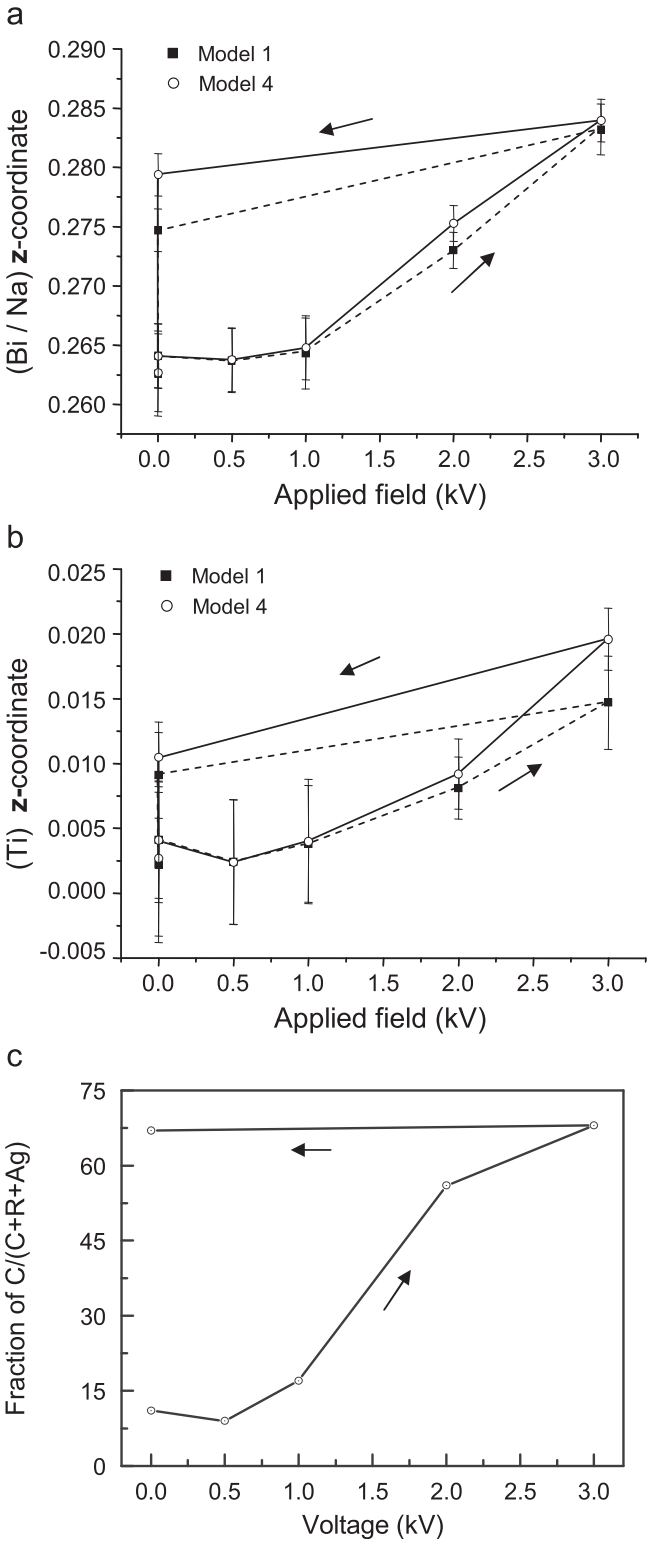

Fig. 4. The refined coordinates of cations (a) and (b) and relative ratio of additional "cubic phase" (c).

above the coercive electric field of the BNT sample based on our ferroelectric measurements. Under such an applied electric field, it seems likely that most of the domains might become aligned and thus apparent PO significant. Including a preferred orientation parameter (Model 2 and later Model 4) therefore significantly improved the fitting statistic parameters. This improvement is particularly noticeable at 3 kV.

On the other hand, it is important to know that the introduction of the PO parameter does not significantly change the refinement results as regards the refined fractional co-ordinate positions. In practice, the refined positions for the Bi/Na and Ti ions (see Table 1 and Fig. 4) remain the same to within 3 standard deviations whether PO is refined or not. This allows us to introduce the PO parameter in this work to improve the refinement statistics parameters. Besides, the variation in the relatively intensity of diffraction peaks originates not only from the PO but also from other factors, such as different off-sets. It is quite difficult to separate such effects from each other unless a large number of refinements are carried out using diffraction patterns collected at different rotation angles and under different applied electric fields. This is well beyond the scope of the current paper.

In Model 3, the additional "cubic phase" designed to model the octahedral tilt twin disorder is introduced but without the preferred orientation parameter. The addition of this "cubic phase" reflects the evolution of the fraction of the IGMS within the rhombohedral matrix (cf. Figs. 1 and 2 in Ref. [14]). The refinement parameters are all considerably improved (see Fig. 2(b) and (c) as well as Table 1). One thing to note is that the fraction of the additional parent phase affects the refined *x*- and *y*-coordinates of the oxygen atoms. This is because the oxygen atoms contribute substantially to the superstructure reflections and if we change the relative amount of the two phases we are in fact changing the relative intensities of the superstructure to parent structure reflections for the superstructure phase. However, we can get an estimate of this by comparing the four models and the difference between them is not significant (see Table 1).

In Model 4 we additionally introduced PO. Fig. 2(d) presents the Model 4 refinement result for the diffraction pattern collected at 3 kV. As can be seen this last approach leads to a much improved fit of the diffraction pattern but with virtually the same fractional co-ordinate parameters as obtained using Model 1. Where we previously had some under calculated parent reflections and mismatched peaks (see e.g., the arrows indicated in Fig. 2), we now have a rather good fit to the data. Reasonable refinement statistics were then obtained for all patterns using Model 4 (Table 1).

The following discussion is based on the refinement results carried out via Model 4. Note that the four refined fractional co-ordinate parameters have quite similar values and also behave very similarly as a function of applied voltage regardless of whether or not the additional "cubic" phase is added, we are thus confident that the refined structural trends as a function of applied voltage shown in Fig. 4(a) and (b) represent real field-induced structural changes.

5. Discussion and conclusions

Fig. 4(a) and (b) show the measured off-centre displacements of the cations relative to the oxygen anion array under the effect of the applied electric field. The displacement of the cations increases systematically with respect to the external electric field. It is intriguing, but perhaps not surprising, that the refined *z*-parameters, $z_{Bi/Na}$ and z_{Ti}, display hysteresis like behaviour and do not entirely return (or relax) to their initial values (see Table 1 and Fig. 4) upon removal of the applied electric field, giving a remanent polarisation as well as a remanent strain. Once the sample is depolarised by heating above the Curie temperature, all the refinement parameters completely returned to the original points (the data has been collected and refined in this work but does not present here). For instance, $z_{Bi/Na}=0.2627(11)$, $z_{Ti}=0.0027$ and the phase fraction of the "cubic" phase ~11% after heat treatment above the Curie temperature. This phenomenon is consistent with, as well as responsible for, the spontaneous polarisation-field and strain-field behaviour of this ferroelectric material. It also shows the same trend as other ferroelectric materials, such as lead zirconate titanate (PZT) [20], in which the nanostructure varies with respect to the external electrical field and partially relax after removal of the electrical field. Removal of the observed remanent strain and polarisation requires either switching of the sign of the applied electric field or annealing at elevated temperature to get the cations to return to their original position.

A further observation is that as the field is increased we need to increase the amount of the additional "cubic phase" in order to get a good fit to the overall pattern. This would seem to indicate that the volume of the *R3c* superstructure domains are getting smaller relative to the volume of the *Pnma* type interface regions as the applied field increases. This is, however, necessarily a tentative conclusion as the neutron diffraction patterns of BNT cannot really be appropriately modelled given the existence of fine scale microstructure. Nevertheless, taking into consideration the facts provided by Dorcet et al. [13–16], it seems highly possible that the proportion of the orthorhombic *Pnma* structure at the $[1\,0\,0]_p$ twin plane interfaces (see Fig. 1(a)) increases systematically with increasing applied electric field and consequently leads to something resembling a phase transition into an "orthorhombic" *Pnma* structure intergrown within an *R3c* rhombohedral phase matrix.

Fig. 4(c) shows the refined relative ratio of "cubic phase" to the total refined phase composition in sum ("cubic"+rhombohedral+Ag), where the Ag phase fraction remains unchanged with increasing external electric field. This ratio evolution exhibits much stronger nonlinear behaviour (Fig. 4(c)) than the cation displacements once the electric field increases (c.f. with Fig. 4(a) and (b)). This suggests that the electric field induced change in the intergrown structure may make a nonlinear contribution towards the total electric field induced polarisation and strain. It is suggested that the large polarisation-field hysteresis loop and large strain-field butterfly loop of BNT originates from the field induced change in the microstructure along the $[1\,1\,1]_p$ direction i.e., the *z* direction in the rhombohedral phase [21]. First, the intergrown structural regions alter the amount of octahedral tilting along the $[1\,1\,1]_p$ direction in the rhombohedral matrix phase, consequently resulting in considerable change in the induced polarisation and strain along this direction. Second, the growth of IGMS locally transforms the original rhombohedral phase to a local orthorhombic phase. The rhombohedral and orthorhombic phases have different local polarisation directions and the corresponding polarisation and strain are hence changed. Note that the amount of the additional "cubic phase" still remains quite high even after withdrawal of the applied electric field (see Table 1 and Fig. 4(c)). The trend of the ratio variation is more consistent with the observed butterfly strain-field loop [21]. These results, in conjunction with those of Dorcet et al. [13–16], suggest that electric field induced changes in octahedral tilt faulting [15] and associated micro-structure may make a significant contribution to the observed large piezoelectric effect in BNT. This suggested viewpoint needs further evidence to be convincing and will be a subject for future investigation. Finally, it is commonly observed that an applied electric field induces texture

in the form of preferred orientation, suggesting that domain wall motion also contributes to the observed polarisation and strain loops, in good agreement with previous work on ferroelectric materials [17,18].

In conclusion, an *in situ* neutron diffraction study of BNT ceramics under an applied external electric field shows field induced atomic displacements as well as changes in fine scale microstructure that appear to have a significant influence on the measured ferroelectric and piezoelectric properties. A detailed understanding of this fine scale micro- to nano-structure and its behaviour under an applied electric field is required to fully understand the piezo-response behaviour of BNT.

Acknowledgments

YL, YPG and RLW thank the Australian Research Council (ARC) for financial support in the form of ARC Discovery Grants. YL also appreciates support from the ARC Future Fellowships programme. The authors also acknowledge the Australian Nuclear Science and Technology Organisation (ANSTO) for making the neutron-beam facilities available.

References

[1] W.F. Liu, X.B. Ren, Phys. Rev. Lett. 103 (2009) 257602.
[2] M. Ahart, M. Somayazulu, R.E. Cohen, P. Ganesh, P. Dera, H.K. Mao, R.J. Hemley, Y. Ren, P. Liermann, Z.G. Wu, Nature 451 (2008) 545–548.
[3] G.O. Jones, P.A. Thomas, Acta Crystallogr., Sect. B 58 (2002) 168–178.
[4] T. Takenaka, H. Ngata, Y. Hiruma, Jpn. J. Appl. Phys. 47 (2008) 3787–3801.
[5] C.S. Tu, S.H. Huang, C.S. Ku, H.Y. Lee, R.R. Chen, V.H. Schmidt, H. Luo, Appl. Phys. Lett. 96 (2010) 062903.
[6] M. Spreitzer, M. Valant, D. Suvorov, J. Mater. Chem. 17 (2007) 185–192.
[7] J. Kreisel, P. Bouvier, B. Dkhil, P.A. Thomas, A.M. Glazer, T.R. Welberry, B. Chaabane, M. Mezouar, Phys. Rev. B 68 (2003) 014113.
[8] M.J. Wu, Y.Q. Lu, et al., J. Am. Ceram. Soc. 90 (2007) 3642–3645.
[9] P.A. Thomas, J. Kreisel, A.M. Glazer, P. Bouvier, Q.Z. Jiang, R. Smith, Z. Kristallogr. 220 (2005) 717–725.
[10] W.A. Dollase, J. Appl. Crystallogr. 19 (1986) 267–272.
[11] B.A. Hunter, Commission Powder Diffr. Newsletter 20 (1998) 21.
[12] A.D. Rae, J.G. Thompson, R.L. Withers, A.C. Willis, Acta Crystallogr. B46 (1990) 474–487.
[13] V. Dorcet, P. Marchet, G. Trolliard, J. Eur. Ceram. Soc. 27 (2007) 4371–4374.
[14] V. Dorcet, G. Trolliard, Acta Mater. 56 (2008) 1753–1761.
[15] V. Dorcet, G. Trolliard, P. Boullay, J. Magn. Magn. Mater. 321 (2009) 1758–1761.
[16] G. Trolliard, V. Dorcet, Chem. Mater. 20 (2008) 5074–5082.
[17] J. Wang, Y. Liu, R.L. Withers, A. Studer, Q. Li, L. Norén, Y.P. Guo, J. Appl. Phys. 110 (2011) 084114.
[18] J.E. Daniels, W. Jo, J. Rödel, J.L. Jones, Appl. Phys. Lett. 95 (2009) 032904.
[19] J.V. Bernier, M.P. Miller, J. Appl. Crystallogr. 39 (2006) 358–368.
[20] M. Hinterstein, M. Hoelzel, H. Kungl, M.J. Hoffmann, H. Ehrenberg, H. Fuess, Z. Kristallogr. 226 (9) (2011) 155–162.
[21] M. Suzuki, A. Morishita, Y. Kitanaka, Y. Noguchi, M. Miyayama, Jpn. J. Appl. Phys. 49 (2010). 09MD09-1/5.